RSC Publishing Faraday Discussions

Structural transition pathway and bipolar switching of the GeTe-Sb_2Te_3 superlattice as interfacial phase change memory

Journal:	*Faraday Discussions*
Manuscript ID	FD-ART-05-2018-000093.R1
Article Type:	Paper
Date Submitted by the Author:	02-Jul-2018

Complete List of Authors:	Inoue, Nobuki; National Institute of Advanced Industrial Science and Technology Nakamura, Hisao; National Institute of Advanced Industrial Science and Technology,

SCHOLARONE™
Manuscripts

Structural transition pathway and bipolar switching of the GeTe–Sb_2Te_3 superlattice as interfacial phase-change memory

*Nobuki Inoue and Hisao Nakamura**

CD-FMat, National Institute of Advanced Industrial Science and Technology (AIST), 1-1-1 Umezono, Tsukuba Central 2, Tsukuba, Ibaraki 305-8568, Japan

ABSTRACT. We investigated the resistive switching mechanism between the high-resistance state (HRS) and the low-resistance state (LRS) of the GeTe–Sb_2Te_3 (GST) superlattice. First-principles calculations were performed to identify the structural transition pathway and to evaluate the current–voltage (*I*–*V*) characteristics of the GST device cell. After determining the atomistic structures of the stable structural phases of the GST superlattice, we found the structural transition pathways and the transition states of possible elementary processes in the device, which consisted of a thin film of GST superlattice and semi-infinite electrodes. The calculations of the *I*–*V* characteristics were examined to identify the HRS and the LRS, and the results reasonably agreed with those of our previous study (H. Nakamura *et al*., *Nanoscale*, **9**, 9286 (2017)). The calculated HRS/LRS and analysis of the transition states of the pathways suggest that a bipolar switching mode dominated by the electric-field effect is possible.

Introduction

The main memory systems used in modern computers, SRAM and DRAM, are volatile. Volatile memory requires electric power to store and update information. Currently, society needs a battery-less information storage technology to enable the development of sensors, Internet of Things devices, etc. [1] Furthermore, more efficient CPUs based on memristive or neurocomputational chip are urgently needed to process big data and apply data science technologies. [2, 3] Therefore, the development of ultra-low-power and fast-switching nonvolatile memory technologies has become one of the most important research targets in the materials science and electronic device communities. [4]

Phase-change memory (PCM) is one of the candidates for next-generation nonvolatile memory technology because of the low variation of its resistance values over many read/write cycles. [5, 6] Chalcogenide crystals have often been used as phase-change materials, where the difference in electrical resistance between the crystalline and amorphous states is used for information storage. Digital versatile disc random access memory (DVD-RAM) is one example of PCM, where the phase transition is triggered by heat generated by optical (laser) input. [7, 8] In applications such as electric nonvolatile memory, alloys composed of Ge, Sb, and Te (GST) are promising materials for the resistive switching layer (RSL) of the PCM device, where the resistance switches by joule heating. However, the loss of enthalpy in heating-based switching is generally large because the entropy (and free energy) of the amorphous and crystalline phases differs dramatically.

Recently, a GST superlattice that consists of an alternate stacking of hexagonal Sb_2Te_3 quintuple layers (QLs) and rock salt-type GeTe layers bound by van der Waals forces was developed as a PCM. [9] This GST superlattice (GST-SL) is represented as $(Sb_2Te_3)_m(GeTe)_n$, where the indices m and n, which characterize the numbers of QL blocks and GeTe layers, respectively, are tunable through recent advanced fabrication techniques. [10] Here, we denote the QL block $(Sb_2Te_3)_m$ as $(QL)_m$.

The phase transition of the GST-SL is a crystal–crystal structural transition that has been confirmed by the following experimental findings. [9] First, the evaluated loss of entropy is reduced by 95% for GST-SL compared with that of the related alloy. Second, a large deviation of the electrical resistance from Ohm's law is observed. Third, the observed change in the electrical resistance is very rapid compared with that induced by melting of the alloy. To emphasize the difference between the phase transition mechanism of GST-SL and that of standard PCMs, we hereafter refer to the former as an interfacial PCM (iPCM).

Although the crystal–crystal phase transition is the key feature of iPCM, details of the dynamics of resistive switching processes such as structural transition pathways are still under debate. Several

energetically and thermodynamically stable structures of GST-SL with or without intermixing of the QL and GeTe layers have been reported. [11-18] Three structural phases, which are termed the inverted Petrov (IP), ferro-GeTe (FGT), and Petrov (P) phases, have been suggested by first-principles calculations when intermixing was not considered. [16] The IP phase has a Te–Ge–Ge–Te sequence of each GeTe layer, whereas the P phase presents a Ge–Te–Te–Ge sequence. The FGT phase has a Te–Ge–Te–Ge order (or, equivalently, Ge–Te–Ge–Te). The P (FGT) phase is further classified by the nature of the vertical flip of the Ge layer in the IP structure, which is termed as P(v) [FGT(v)]] for the vertical flip only and that followed by lateral motion is denoted as P(vl) [FGT(vl)]. This lateral motion is related to a thermal relaxation process; hence, P(vl) [FGT(vl)] is thermally more stable than P(v) [FGT(v)]. [17] Strong interlayer mixing of the QL blocks and the GeTe layers in GST-SL, which partially breaks the perfect reciprocal stacking, has also been reported by several research groups. [14, 19] However, strong intermixing cannot explain the observed cyclic and rapid resistive switching of iPCM because the occurrence of intermixing is almost equivalent to melting of the interface. After formation of the intermixing region, Ge or Te atoms lack sufficient space to change their atomic positions without melt/crystallization, which requires a nonlocal structural change. Therefore, resistive switching of the iPCM is reasonably expected to be dominated by a local (GeTe) structural change within the region of QL/GeTe stacking.

Very recently, we reported first-principles calculations related to the electric transport properties of the aforementioned structural phases, where the RSL was $[(QL)_2(GeTe)_2]_3$, which was connected to W electrodes.[20] We use the notation $[(m,n)]$ to represent the unit cell of the reciprocally stacked $(QL)_m(GeTe)_n$GST-SL. When a number, l, of such units are stacked, we refer to the resulting film as $[(m,n)]_l$. In this notation, the GST-SL bulk of the $[(m,n)]$ unit cell is $[(m,n)]_\infty$. On the basis of calculated current–voltage (I–V) characteristics, the possible low-resistance states (LRSs) were identified as the P(v) and FGT(vl) structures, whereas the high-resistance state (HRS) was the IP structure. Because FGT(vl) structures are thermally more stable than the P(v) and FGT(v) structures, the structural transition from IP to FGT(vl) is a more promising pathway for resistive switching dynamics. These theoretical results suggest that SET/RESET operations can be controlled via a bipolar voltage sweep because only the FGT structure is oriented (i.e., it has a spatially asymmetric atomic configuration). However, to clarify the resistive switching mechanism and enable ultra-low-power operation, elucidation of the potential energy profile along the transition pathway—in particular, the potential energy barrier of each elementary process—is necessary.

In the present study, we carried out calculations of the potential energy profiles of possible structural transition pathways from the IP structure to both the P(v) and the FGT(vl) structures to understand the SET operation of an iPCM. The potential energy profile is evaluated by calculation of the entire iPCM device, which consists of the GST-SL and, explicitly, a semi-infinite W electrode. This

approach is important for modeling the dynamics of the device and for validating the results by comparing them with those obtained from calculations of the GST-SL bulk, because the Fermi level of the system is determined by that of the electrodes. In addition, we include the spin–orbit (SO) interaction, which is often omitted in total energy calculations, to evaluate the potential energy profile and to show the effect on Ge/Te switching. The SO interaction strongly affects the transport properties of the LRS, especially those for FGT(vl), as well as the electronic properties of the interfacial states of the QL and GeTe layers in the IP structure. Therefore, omitting the effect of SO interaction on the potential energy profile is not necessarily valid. In the present model, we adopt five pathways as candidates and calculate all possible transition states and potential energy barriers along each elementary process, which is a subpart of the transition pathway, because the transition pathway of the SET process does not necessarily involve single-step dynamics. We then evaluate the *I–V* characteristic of each "intermediate" structure along a given path as well as the voltage effects; the results provide useful insights into the contribution of self-heating (local heating) to switching.

Setting Up the Models of the iPCM Device

To set up the device model and examine the effect of electrodes, we carried out procedures similar to those described in Ref. [[20]]. The IP, FGT(v), FGT(vl), P(v), and P(vl) structures are known to be energetically stable[17] and were examined as the possible HRS or LRS. We introduced a (2,2) superlattice as the unit of the RSL. First, the unit cell of (2,2) GST-SL bulk was determined by density functional theory (DFT) calculations with relaxation of all atoms in the unit cell, where the SO interaction is not included. The atomic positions of each structure are listed in Fig. 1. Here, the lattice constant of the *a*- and *b*-axes was taken as 4.19 Å, as given in Ref. [[20]], and that of the *c*-axis was 28.33 Å. The resulting energies per each unit cell are shown in the first column of Table 1. As the next step, we introduced body-centered cubic (bcc) W(111) electrodes onto the left and right sides of the RSL and carried out DFT calculations. The RSL consisted of $(2,2)_1(QL)_2$, where the last $(QL)_2$ block was introduced to obtain a symmetric junction. Thus, the structure of the device cell is expressed as $W/(2,2)_1(QL)_2/W$. Fourteen atomic layers of W atoms were included as the left- and right-side electrodes, respectively. Here, the *a* and *b* lattice constants were fixed to match those of the GST-SL bulk and the gap-distance of the electrodes was fixed at 74.13 Å on the basis of estimates in our previous study Ref. [[20]] and the calculation results for (2,2) GST-SL bulk.

To define the common device cell size to all the structural phases of GST-SL, we relaxed the atoms of $(2,2)_1(QL)_2$ and the neighboring three W atoms in the device cell of the IP structure. We then fixed all atoms of W electrodes and determined the atomic positions by relaxing only the central $(1,2)_1(QL)_1$ region in the device for the other structures. Notably, the atomic positions in the outermost region of the electrodes were taken from those of W bulk. Schematics of the device cells

are shown in Fig. 2. The resulting energies of the device cell, where the SO effect was omitted, are listed in the third column in Table 1, and we find that the atomic configurations of the attached electrodes are very similar to the atomic configurations of the RSL. Finally, we recalculated the total energies of the device cells using the nonequilibrium Green's function DFT (NEGF-DFT) method to include the explicit boundary condition; i.e., the device cell was taken as the scattering region and was connected to the semi-infinite electrodes.[21-23] We checked the resulting energies per cell by DFT and NEGF-DFT and found that the difference was less than 0.02 eV.

The relative energy differences among the IP, FGT, and P phases of the unit cell of GST-SL bulk are approximately the same as those among the IP, FGT, and P phases of the iPCM device cell when the SO interaction was omitted. For instance, the energy difference between the IP and FGT(vl) structures is −0.09 eV and −0.17 eV for the unit cell of the (2,2) GST-SL bulk and the iPCM device cell, respectively. Next, we calculated the total energies with inclusion of the SO interaction; the results are also listed in Table I, where the second and fourth columns present the total energies of the GST-SL bulk and the iPCM device cell, respectively. Comparing the results, we find that the potential energy profiles of the energetically stable structures are affected by the SO interaction energy. In contrast, the potential energy profiles obtained by calculations of the GST-SL bulk and the device cell are quite similar. The FGT(vl) and P(vl) are still much more energetically stable than FGT(v) and P(v), as expected. Here, we note that the SO interaction at the W(111) surface is large and that our calculations show that the SO interaction destabilizes the device cell of the FGT(v) and P(v) structures by relaxing atoms of a few top layers of the electrodes. The vertical flip of Ge and Te atoms substantially changes the thickness of the RSL. Thus, overestimation of SO interaction energy between the W electrode and the outermost QL will be enhanced when the volume of the entire device cell is fixed. We accept this overestimation as a limitation of the model to perform consistent calculations of the *I–V* characteristics for comparing the HRS and the LRS. However, the atomic positions in the QLs inside the device are not affected by the vertical flip of the Ge and Te atoms. Furthermore, we do not observe any energetic destabilization of the QLs inside the RSL as a result of the SO interaction. Thus, we conclude that our procedure used to determine the structures of the device cell models is reasonable for the present purpose.

Structural Transition Pathways and Potential Energy Profiles

We now analyze details of the structural transition pathways related to the resistive switching. The resistive switching is mainly dominated by the structural transition in the $(GeTe)_2$ layer. The following two hypotheses are often considered as dynamics of the SET operation (i.e., the pathway from HRS to LRS). The first hypothesis is that a structural change from IP to FGT(v) occurs, as proposed by Tominaga *et al*.[24, 25]; the second hypothesis is that IP changes to P(v), as proposed by Ohyagi et al.[15, 26] However, the recent free-energy analysis of GST-SL bulk by Yu and Robertson

shows that the HRS is the IP phase and that the LRS should be the FGT(vl) structure.[17] This hypothesis is supported by our recently reported calculated *I*–*V* characteristics. The structural change in the former two cases, i.e., IP → FGT(v) and IP → P(v), assumes that the transition pathway consists of only a single elementary process: a vertical flip motion of Ge and Te atoms along the *c*-axis direction. That is, the potential energy profile has a single energy barrier along the reaction coordinate. However, the lateral motions of Ge and Te atoms, which are parallel to the GeTe/QL interface, are required when the LRS is the FGT(vl) structure, i.e., the transition pathway must consist of two (or more) elementary processes as two-step dynamics. In two-step dynamics, the vertical flip and lateral motions are the elementary processes. Here, we assume that no global atomistic reconfiguration is induced by a large defect region or by intermixing of the interfaces. As previously stated, the SET operation can occur as single-step dynamics via the vertical flip as IP → FGT(v) or IP → P(v), or as two step-dynamics such as IP → FGT(v) → FGT(vl) or IP → P(v) → P(vl). Hereafter, we label the elementary processes IP → FGT(v), IP → P(v), FGT(v) → P(v), FGT(v) → FGT(vl), and P(v) → P(vl) as V1, V2, V3, L1, and L2, respectively. In addition, we refer to the TS structure corresponding to the elementary process *X* as TS(*X*), where *X* is V1, V2, V3, L1, or L2. Although we simply state the elementary processes by lateral motion as L1 and L2, two more precise lateral motions are possible: the overhead motion and the snake-like motion, as shown in Ref. [[17]]. In the overhead motion, Ge and Te atoms cross each other. In contrast, Ge and Te atoms move along almost the same directions in the *a*–*b* plane (i.e., parallel to the QL/GeTe interface) in the snake-like motion. Detailed schematics of the vertical flip and lateral motions are shown in Fig. 3. For example, the transition pathway of IP → P(vl) is divided into two or more elementary processes such as V2 → L2 or V1 → V3 → L2, and then L2 to L2 (overhead) or L2 (snake-like) is identified.

First, we searched the TS structures and evaluated their potential energy profiles by adopting the (2,2) GST-SL bulk system. We applied the nudged elastic band (NEB) method and the climbing image NEB (CI-NEB) method[27, 28] with and without the SO interaction. The calculated barrier height of TS(V1), TS(V2), TS(V3), TS(L1), and TS(L2) are listed in the first and second columns in Table 2. The SO effect on the potential energies of the TSs is very small when the GST-SL bulk system is adopted. The energy of TS(L1) by overhead motion is much higher (ca. 1.5 eV) than that of snake-like motion, and L2 by overhead motion is almost forbidden; i.e., the lateral motion of L1 and L2 should be snake-like. Hereafter, we consider only snake-like lateral motions for L1 and L2.

As the next step, we adopted the device cell to determine the TS structures, where the NEB/CI-NEB was combined with NEGF-DFT. The obtained TS structures are almost the same as those of the GST-SL bulk. The resulting structures of TS(V1), TS(V2), TS(V3), TS(L1), and TS(L2) are presented in Fig. 4, which focuses only on the GeTe block. A comparison of Figs. 3 and 4 reveals that the TS structure from the IP phase followed by the vertical flip motion is only in the middle position of the inverting umbrella of GeTe and that the moved Ge and Te atoms are located on

almost the same plane. The potential energies of TSs related to the vertical flip motion are always higher than those of the TSs corresponding to lateral motions. This relationship is quite reasonable because Ge atoms must pass through a triangular region formed by nearest Te atoms during the vertical flip motion and the interatomic distances among these atoms in the triangular region are very short. The potential energies determined by calculations of the device cell without and with consideration of the SO interaction are listed for comparison in the third and fourth columns of Table 2, respectively. Again, the results for GST-SL bulk are shown to be a good approximation for those of the device cell for the TS structures. The V2 process requires twice the energy as the other elementary processes; thus, V1 is strongly preferred as the initial SET operation. That is, single-step dynamics from IP to P(v) requires sufficiently large joule heat. In addition, the activation energy of L1 is only 25% of that of V1; hence, thermal relaxation from FGT(v) to FGT(vl) should be considered in the entire dynamics. Therefore, the SET operation is reasonably considered to be caused by the change from IP to FGT(vl) via two-step dynamics.

Electric Transport Properties of HRS, LRS, and Intermediate States during Structural Transition

Thus far, we have assumed that the structural phases of GeTe for the HRS and for the LRS are the same as those suggested in our previous study. We elucidated the transition pathways and related TSs between the IP phase and the other stable states as the pathway from the HRS to the LRS (i.e., the dynamics of the SET operation). However, the present model, W/$(2,2)_1(QL)_2$/W, differs slightly from the model adopted in Ref [[20]], where the RSL was $(2,2)_3(QL)_2$. Hence, we need to check the validity of our assumption by calculating the *I–V* characteristics of the device. In addition, comparing the electric current at the TSs with those of the HRS and the LRS would provide a rough estimate of the change in joule heat generated during the SET operation, which occurs via acceleration of the structural transition. When the dominant electric current is ballistic, it can be represented using the transmission coefficient $T(V, E)$[29]:

$$I = \frac{2e}{h}\int_{-\infty}^{+\infty} T\,(E,V)\{f(E-\mu_L) - f(E-\mu_R)\}dE \quad , \qquad (1)$$

where f is the Fermi–Dirac distribution function. The transmission coefficient is evaluated using NEGF-DFT calculations.[21, 22] In the present study, we focus on the *I–V* characteristics only in the low-bias regime to identify the HRS and the LRS. Hence, we adopted a zero-bias approximation to evaluate Green's functions to calculate the *I–V* characteristics. Here, before starting analysis of the *I–V* characteristics, we give a brief comment about validity of the ballistic transport approximation adopted in the present study. The iPCM is the superlattice by reciprocal stacking of the thin QLs and

thin GeTe blocks. In the contrast to the alloy or amorphous, where electrons are trapped and hopping between vacancies, the wavefunctions can be sufficiently delocalized. If concentration of vacancies in the GST-SL is high enough to change the dominant transport mechanism to multiple scattering and/or diffusive transport, the stacked layers should be broken by intermixing. As stated in the previous sections, we consider that characteristic resistive switching of iPCM cannot coexist with such strong intermixing. Furthermore, the device-scale of the iPCM unit is often in 10 nm scale, which is the quantum transport regime, i.e, coherent process is good first approximation to analyze HRS/LRS. Validity of ballistic transport approximation was also supported by analyzing thickness-dependence of resistance in Ref. [[20]]

The calculated *I–V* curves are shown in Figs. 5(a) and 5(b), where the former is the result obtained without including the SO interaction, and the latter is obtained with inclusion of the SO interaction. From Figs. 5(a) and 5(b), the IP structure is identified as the HRS. This result is consistent with the previous results. We now focus on identifying the LRS. Because the P(vl) and FGT(vl) phases are energetically as stable as the IP phase, they are the most promising LRS candidates. The *I–V* curves for the P(vl) and FGT(vl) phases are plotted by blue and red solid lines in Figs. 4(a) and (b). The SO effect rapidly increases the electric current for the FGT(vl) structure, and the ON/OFF electric current ratio (i.e., the ratio between the electric current for FGT(vl) and that for IP) is sufficiently large to define distinct resistive switching. Thus, we conclude that the FGT(vl) structure can be the LRS, as suggested by our previous work. In contrast, the SO interaction does not change the tendency of the *I–V* characteristics of the P(v) and P(vl) structures.

To understand more details of electric transport properties, we evaluated the transmission coefficient *T(E,V=0)* in Eq. (1) at each k-points of the lateral $\vec{k}_{//}$ along M−Γ−K line. Then we plotted obtained band structure of the transmission coefficient, $T(E,\vec{k}_{//})$, of the three structures, IP, FGT(v), and FGT(vl), respectively. The results are shown in the Supporting Information SI. 1. Since the transmission coefficient represents the transmission probability of an electron through the RSL with its energy E, it relates to the wavefunctions of the electric transport channels between the source and drain electrodes. When the energy is close to E_F, the transmission coefficient is small along the Γ−K line for all the structures. Then $T(E,\vec{k}_{//})$ increases as one moves away from the Γ to M point. The value of $T(E,\vec{k}_{//})$ of FGT(vl) increases rapidly comparing to those of the other two structures in the region below E_F. These findings show that the resistive switching is dominated by the transport channels away from Γ point and their energies are lower than E_F. The latter is consistent with the fact that Sb_2Te_3 is p-type narrow gap semiconductor.[30].

We now analyze the electric current at the TSs. All of the TSs have much lower resistance values than the HRSs and LRSs (i.e., IP, FGT(v), FGT(vl), P(v), and P(vl)). We evaluated the average joule

heat Q using Joule's law. Here, we omitted the deviation from Ohm's law caused by the voltage dependence of the derivative conductance and set the resistance to the inverse of the derivative conductance at $V = 0$. This approach thus provides a very crude approximation because we omitted electron–phonon interaction to calculate the electric current and because the deviation from Ohm's law is not necessarily negligible, especially in the high-bias regime. However, such an analysis should still be useful for discussing the ability of heating (current-driven) to accelerate elementary processes in each structural transition pathway. Because the SET operation via IP → FGT(vl), which is a two-step dynamics process consisting of V1 and L1 elementary processes, is potentially electric-field driven (i.e., bipolar mode[31]), analysis of the I–V characteristics and the change of Q during V1 and L1 should be interesting.

We obtained the largest value of Q for TS(V1), and all of the present TSs gave much larger Q values than those of the IP, FGT(v), and FGT(vl) structures. The relative values of heat, where we set the value of IP (i.e., HRS) to 1, are 2.15, 1.51, 2.76, and 1.63 for TS(V1), FGT(V), TS(L1), and FGT(vl), respectively. Thus, large excessive heat is generated during the V1 process even if the V1 process is promoted by the electric-field effect. This excessive heat must subsequently be dissipated. As a result, some of the dissipated heat accelerates the lateral motion; i.e., sufficient energy is provided to overcome the potential energy barrier of the L1 process, particularly, snake-like motion, where the barrier height of the L1 process is only 0.33 eV (See Table 2). Hence, the second step in the two-step dynamics, i.e., lateral motion, does not necessarily require direct assist of electric-field effect. This scenario is consistent with the mechanism suggested by Yu and Robertson, who speculated that the lateral motion provides a quick thermal relaxation process.[17]

Notably, the present analysis explains why the L1 process is as important as the V1 process in the bipolar (SET) mode, even though the lateral motion is almost perpendicular to the direction of the voltage drop or electric current flow.

Finally, we demonstrate suppression of the potential energy barrier of the V1 process by applying a bias voltage. When the DC bias is applied, an electronic state of the device is a stationary nonequilibrium state; hence, the force acting on ions by electrons is defined as the derivative of the momentum with respect to time.[32, 33] Within the NEGF-DFT formalism, this mean-field force is expressed as

$$F_{ci} = -\mathrm{Tr}\left[\frac{\partial \mathbf{H}(V)}{\partial R}\cdot\frac{1}{2\pi i}\int \mathbf{G}^{<}(E,V)\,dE\right] + \mathrm{Tr}\left[\frac{\partial \mathbf{S}}{\partial R}\cdot\frac{1}{2\pi i}\int E\mathbf{G}^{<}(E,V)\,dE\right] \qquad (2)$$

where $\frac{\partial H}{\partial R}$ and $\frac{\partial S}{\partial R}$ are the derivative of the Hamiltonian and overlap matrices by an ion position. $\boldsymbol{G}^{<}$ is the lesser Green's function matrix.[34] Note that $\mathbf{H}$ and $\boldsymbol{G}^{<}$ in Eq (2) are now determined self-consistently to include voltage bias V explicitly. The force F_{ci} is often called the current-induced force and can be expressed as the sum of the standard equilibrium force (i.e., the force obtained by zero bias), which is related to the derivative of the total electronic energy by ion positions. The nonequilibrium force is then expressed as

$$, \quad F_{neq} = -\mathrm{Tr}\left[\frac{\partial \mathbf{H}}{\partial R}\cdot\frac{1}{2\pi i}\int\left(\mathbf{G}^{<}(E,V)-\mathbf{G}^{<}(E,0)\right)dE\right]+\mathrm{Tr}\left[\frac{\partial \mathbf{S}}{\partial R}\cdot\frac{1}{2\pi i}\int E\left(\mathbf{G}^{<}(E,V)-\mathbf{G}^{<}(E,0)\right)dE\right] \quad (3)$$

and the potential energy profile of a biased device, $U_{PES}(s,V)$, is

$$U_{PES}(s,V) = (E_{tot}^{eq}(s) - E_{tot}^{eq}(0)) + \int_0^s ds' F_{neq}(s') \quad (4)$$

where s is the path coordinate obtained from the NEB result, and E_{tot}^{eq} is the total energy of the zero-biased device. F_{neq} is not a conservative force,[35] i.e., the potential energy profile defined by Eq (4) is implicitly path-dependent. However, evaluation of energy suppression of the TS by Eqs. (3) and (4) is useful in analyzing dynamics because the coordinate s is a good first approximation of the transition pathway. As a physical insight, consider that F_{neq} consists of an electrostatic interaction term such as a dipole–inner field interaction and wind-force by electric current flow. The wind-force can be understood as the result of elastic collisions of electric current and ions. Strictly, no unique definition exists to separate F_{neq} into electrostatic and wind-force terms. However, the nonequilibrium force does not include any joule heating effect, which is caused by inelastic scattering of electric current and ions.[36] In this sense, we classify dynamics dominated by current-induced force (or nonequilibrium force) as "electric-field driven." Fully self-consistent NEGF-DFT calculations were carried out along the V1 pathway for V = 1.0 V and V = 1.5 V; U_{PES} was then evaluated by Eq. (4). The energy of TS(V1) decreased by 0.67 eV and 1.05 eV when the bias was V = 1.0 V and V = 1.5 V, respectively. We checked the profiles of voltage drop in the RSL of IP, TS(V1), and FGT(v) structures, respectively, where the bias is 1.5 V. The profile can be calculated by taking difference of the Hartree potential energies between V=0 and V=1.5V. Here the potential energies are averaged over the a and b-axis and is plotted as a function of the coordinate along the transport direction (c-axis). The results are given in Supporting Information, SI. 2. We found that large voltage drop at each QL neighboring to GeTe block and that electric filed is

sufficiently screened in the GeTe layer in all of the structures. Using other words, charge redistribution is confined in QL or GeTe blocks. In Figure 6, we present F_{neq} acting on each atom of GeTe block. Direction of the dominant component of F_{neq} vector is same with that of electric current of IP and TS(V1) and it clearly pushes the vertical flip motion of Ge atom. In contrast, F_{neq} acting on Ge and Te atoms of FGT(v) is relatively small. i.e., the lateral motion relating to L1 process is not electric-field driven. These results are consistent with our scenario of the two-step dynamics and the presented substantial barrier suppression of the V1 process strongly supports our conclusion that the bipolar SET operation is dominant.

Summary

We investigated the structural transition pathway of the SET/RESET operation in an iPCM device with a GST-SL. To identify the HRS, LRS, and the TS for each possible pathway, we investigated the pathways of possible elementary processes of structural changes using the NEB method and evaluated their *I–V* characteristics by first-principles transport calculations. We identified the elementary processes and found that the potential energy profiles along the pathways are almost independent of the existence of electrodes. Although overestimation of the energy by SO interaction destabilizes the interface of the outermost QL and electrodes for FGT(v) and P(v) structures, this overestimation is a limitation of the device model and the approximation method used to calculate the SO energy, where the volume of the entire device cell must be fixed to ensure consistent *I–V* calculations.

The tendency of the *I–V* characteristics presented here agree with those of our previous study, whereas the number of $(GeTe)_2$ blocks in the RSL is different. The resistance of FGT(vl) is sufficiently low, and the energy required for conversion of the IP phase to the FGT(vl) phase, which includes two elementary processes (i.e., two-step dynamics), is much lower than that required for conversion from the IP phase to the P(v) phase, where the latter consists of two or more elementary processes. The evaluated electric current flow and resulting joule heat at the TSs of elementary processes are much larger than those of energetically stable structures. This difference indicates that the structural change requires sufficient electric-field-driven force as the trigger, whereas joule heating substantially accelerates the structural transition during dynamics, especially the lateral motion, i.e., the second elementary process in the two-step dynamics. The calculated potential energy suppression by nonequilibrium force strongly supports this scenario. However, if much greater excessive heat is accumulated rapidly, it may trigger interlayer mixing or melting of the QL and GeTe blocks. Understanding the competitive effects of electric-field and joule heating current (heating) is necessary to identify the threshold between local coherent GeTe switching and interlayer mixing. More explicit calculations that account for defects[37], the rearrangement of atoms[18], and electron–phonon interactions[38] are in progress.

Computational Methods

We performed DFT calculations using the SIESTA package.[39] The NEGF-DFT transport calculations were then performed using the *Smeagol* code[22, 23] to include SO interaction. The exchange-correlation (XC) functional was applied to the local density approximation (LDA). We used the single zeta plus polarization function (SZP)-level basis set for W atoms and the double zeta plus polarization function (DZP) for the other atoms. Monkhorst–Pack k-point sampling was taken as 8 × 8 × 2 points for the standard DFT calculations, whereas we adopted 16 × 16 × 1 for the NEGF-DFT calculations. The self-energy term of the electrodes was determined on the basis of the results for a bcc W bulk system with 16 × 16 × 8 Monkhorst–Pack k-point sampling. The SO coupling terms were evaluated within onsite approximation. Achieving convergence of the *I*–*V* characteristics as well as of the transmission coefficients required a finer k-point sampling. Thus, in the present work, 100 × 100 k-points were taken after the converged density matrix was obtained by NEGF-DFT. All of the *I*–*V* characteristics were evaluated by integrating the zero-bias approximated transmission coefficient over the voltage-dependent bias window.

ACKNOWLEDGMENTS

This work was supported by CREST, JST (Grant No. JPMJCR14F1). The authors would like to express their appreciation Junji Tominaga and Noriyuki Miyata and Yoshihiro Asai at AIST for their valuable discussions.

REFERENCES

1. R. S. Williams, *Computing in Science & Engineering*, 2017, **19**, 7.
2. J. J. S. Yang, D. B. Strukov and D. R. Stewart, *Nat Nanotechnol*, 2013, **8**, 13-24.
3. S. Gaba, P. Sheridan, J. T. Zhou, S. Choi and W. Lu, *Nanoscale*, 2013, **5**, 5872-5878.
4. S. Mittal and J. S. Vetter, *Ieee T Parall Distr*, 2016, **27**, 1537-1550.
5. S. Raoux, *Woodh Pub Ser Elect*, 2014, DOI: 10.1533/9780857098092.2.161, 161-199.
6. S. Raoux, F. Xiong, M. Wuttig and E. Pop, *Mrs Bull*, 2014, **39**, 703-710.
7. N. Kato, Y. Takeda, T. Fukano, T. Motohiro, S. Kawai and H. Kuno, *Jpn J Appl Phys 1*, 1999, **38**, 1707-1708.
8. N. Yamada, E. Ohno, N. Akahira, K. Nishiuchi, K. Nagata and M. Takao, *Jpn J Appl Phys 1*, 1987, **26**, 61-66.
9. R. E. Simpson, P. Fons, A. V. Kolobov, T. Fukaya, M. Krbal, T. Yagi and J. Tominaga, *Nat Nanotechnol*, 2011, **6**, 501-505.
10. J. Tominaga, A. V. Kolobov, P. J. Fons, X. M. Wang, Y. Saito, T. Nakano, M. Hase, S. Murakami, J. Herfort and Y. Takagaki, *Sci Technol Adv Mat*, 2015, **16**, 014402.
11. B. Casarin, A. Caretta, J. Momand, B. J. Kooi, M. A. Verheijen, V. Bragaglia, R. Calarco, M. Chukalina, X. M. Yu, J. Robertson, F. R. L. Lange, M. Wuttig, A. Redaelli, E. Varesi, F. Parmigiani and M. Malvestuto, *Sci Rep-Uk*, 2016, **6**.
12. J. L. F. Da Silva, A. Walsh and H. L. Lee, *Phys Rev B*, 2008, **78**.
13. B. Huang and J. Robertson, *Phys Rev B*, 2012, **85**, 125305.
14. J. Momand, R. N. Wang, J. E. Boschker, M. A. Verheijen, R. Calarco and B. J. Kooi, *Nanoscale*, 2015, **7**, 19136-19143.
15. T. Ohyanagi, M. Kitamura, M. Araidai, S. Kato, N. Takaura and K. Shiraishi, *Appl Phys Lett*, 2014, **104**, 252106.
16. J. Tominaga, A. V. Kolobov, P. Fons, T. Nakano and S. Murakami, *Adv Mater Interfaces*, 2014, **1**, 1300027.
17. X. M. Yu and J. Robertson, *Sci Rep-Uk*, 2015, **5**, 12612.
18. X. M. Yu and J. Robertson, *Sci Rep-Uk*, 2016, **6**, 22353.
19. J. Kalikka, X. L. Zhou, J. Behera, G. Nannicini and R. E. Simpson, *Nanoscale*, 2016, **8**, 18212-18220.
20. H. Nakamura, I. Rungger, S. Sanvito, N. Inoue, J. Tominaga and Y. Asai, *Nanoscale*, 2017, **9**, 9386-9395.
21. H. Nakamura, K. Yamashita, A. R. Rocha and S. Sanvito, *Phys Rev B*, 2008, **78**, 235420.
22. A. R. Rocha, V. M. Garcia-Suarez, S. Bailey, C. Lambert, J. Ferrer and S. Sanvito, *Phys Rev B*, 2006, **73**, 085414.
23. I. Rungger and S. Sanvito, *Phys Rev B*, 2008, **78**, 035407.
24. D. Bang, H. Awano, Y. Saito and J. Tominaga, *Aip Adv*, 2016, **6**.
25. K. Makino, Y. Saito, P. Fons, A. V. Kolobov, T. Nakano, J. Tominaga and M. Hase, *Appl Phys Lett*, 2014, **105**, 151902.
26. T. Ohyanagi, M. Kitamura, M. Tai, M. Kinoshita, T. Morikawa, K. Akita and N. Takaura, *Ecs Transactions*, 2014, **64**, 75-79.
27. G. Henkelman and H. Jonsson, *J Chem Phys*, 2000, **113**, 9978-9985.
28. G. Henkelman, B. P. Uberuaga and H. Jonsson, *J Chem Phys*, 2000, **113**, 9901-9904.
29. S. Datta, *Electronic Transport in Mesoscopic Systems*, Cambridge University Press, 1997.
30. M. Eschbach, E. Mlynczak, J. Kellner, J. Kampmeier, M. Lanius, E. Neumann, C. Weyrich, M. Gehlmann, P. Gospodaric, S. Doring, G. Mussler, N. Demarina, M. Luysberg, G.

Bihlmayer, T. Schapers, L. Plucinski, S. Blugel, M. Morgenstern, C. M. Schneider and D. Grutzmacher, *Nat Commun*, 2015, **6**.
31. T. Shintani, S. Soeya and T. Saiki, *Ecs Transactions*, 2014, **64**, 69-74.
32. M. Di Ventra and S. T. Pantelides, *Phys Rev B*, 2000, **61**, 16207-16212.
33. T. N. Todorov, *J Phys-Condens Mat*, 2001, **13**, 10125-10148.
34. R. X. Zhang, I. Rungger, S. Sanvito and S. M. Hou, *Phys Rev B*, 2011, **84**.
35. T. N. Todorov, D. Dundas and E. J. McEniry, *Phys Rev B*, 2010, **81**.
36. N. Bode, S. V. Kusminskiy, R. Egger and F. von Oppen, *Beilstein J Nanotech*, 2012, **3**, 144-162.
37. B. Huang and J. Robertson, *J Non-Cryst Solids*, 2012, **358**, 2393-2397.
38. H. Nakamura and Y. Asai, *Phys Chem Chem Phys*, 2016, **18**, 8820-8826.
39. J. M. Soler, E. Artacho, J. D. Gale, A. Garcia, J. Junquera, P. Ordejon and D. Sanchez-Portal, *J Phys-Condens Mat*, 2002, **14**, 2745-2779.

Tables

Table 1

Calculated energies of the structures of FGT(v), FGT(vl), P(v), and P(vl) per the unit cell of GST-SL bulk and the iPCM device cell. The first column represents the energies of GST-SL bulk without the SO effect, which is labeled as wo/SO and the second column shows those with including the SO effect, termed as w/SO. The last two columns show the energies of the iPCM device cell. The unit is in eV and the energy of the IP structures is set to zero for both of wo/SO and w/SO.

	GST-SL bulk (wo/SO)	GST-SL bulk (w/SO)	iPCM device (wo/SO)	iPCM device (w /SO)
FGT(v)	0.26	0.58	0.35	0.73
FGT(vl)	-0.09	0.31	-0.17	0.19
P(v)	0.49	1.00	0.79	1.29
P(vl)	-0.06	0.39	-0.14	0.21

Table 2

The potential energy barrier of the elementary processes, V1, V2, V3, L1, and L2.

The first two columns relate to the results by calculations of GST-bulk system while the latter two columns consist of the results obtained by calculations of device cell. The labels wo/SO and w/SO represent that CI-NEB calculations combined with DFT (NEGF-DFT) include SO effect (w/SO) or not (wo/SO). The unit is in eV.

	GST-SL bulk (wo/SO)	GST-SL bulk (w/SO)	iPCM device (wo/SO)	iPCM device (w/SO)
V1	2.60	2.68	2.54	2.63
V2	4.94	5.05	4.85	4.76
V3	2.47	2.42	2.48	2.34
L1 (overhead)	2.20	2.19	Not Converged	Not Converged
L1 (snake-like)	0.59	0.57	0.39	0.33
L2 (snake-like)	1.22	1.14	1.20	1.05

Figure captions

Figure 1

Structures of the [(2,2)] cell of GST-SL bulk. In the upper right, the directions of a, b, and c-axes are given for reference. The purple, dark yellow and the orange balls represent Ge,Te and Sb atoms, respectively, while the atoms on the boundary of the unit cell (light green lines), which belong to the adjacent cell, are shown by the lighter color for convenience. The most left panel is the IP structure labeled as IP. The red square indicates the GeTe block, where the transitions to the other structural phase are characterized. The four structures, FGT(v), FGT(vl), P(v), and P(vl) are listed in the right panel, where only the GeTe block is presented.

Figure 2

Left panel: schematic picture of the iPCM device cell labeled as $W/[(2,2)]_1(QL)_2$ /W. Labels of atomic species are summarized in the inset. The red enclosing represents GeTe block, where structural change is triggered. Right panel: possible structures of GeTe block.

Figure 3

The schematic pictures of the vertical flip and lateral (snake-like/overhead) motions. The top and side views of $(GeTe)_2$ region are shown for the eye-guide. The color and labels of the atoms are same with those used in Figure 1. The directions of the a, b, and c-axes are represented by the red, green and blue arrows, respectively to define the top and side view in (a). The vertical flip, lateral (snake-like), and lateral (overhead) motions, are shown in (b), (c), (d), respectively. The light blue allows indicate the atomic displacements along each motion.

Figure 4

Structures of the $(GeTe)_2$ block in the device for the transition states, TS(V1), TS(V2), TS(V3), TS(L1), and TS(L2), respectively. The definition of colors to identify the Ge and Te atoms are the same with those adopted in Figure 1.

Figure 5

Current-voltage characteristics of the possible device structures of the inverted Petrov, Petrov, and Ferro-GeTe phases as well as the transitions states of the elementary processes for the structural transition pathways. The label of each structure and relating I-V curve is also summarized in the legend of the Figure. (a) Results without SO effect, (b) Results including SO effect.

Figure 6

Nonequilibrium force acting on Ge and Te atoms in GeTe block. Each allow represents the force vector. The applied bias is 1.5 Volt and the direction of electric current is also given as reference. The left, middle, and right panels are IP, TS(V1), and FGT(v), respectively. The color and labels of the atoms are same with those used in Figure 1.

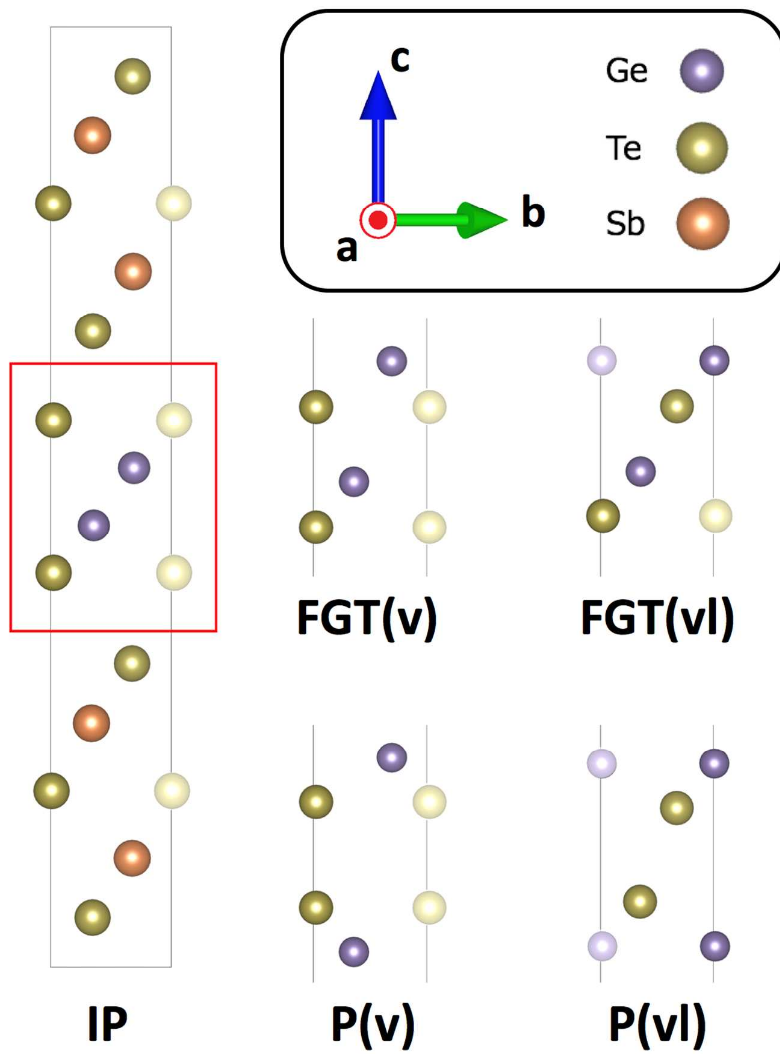

Figure 1

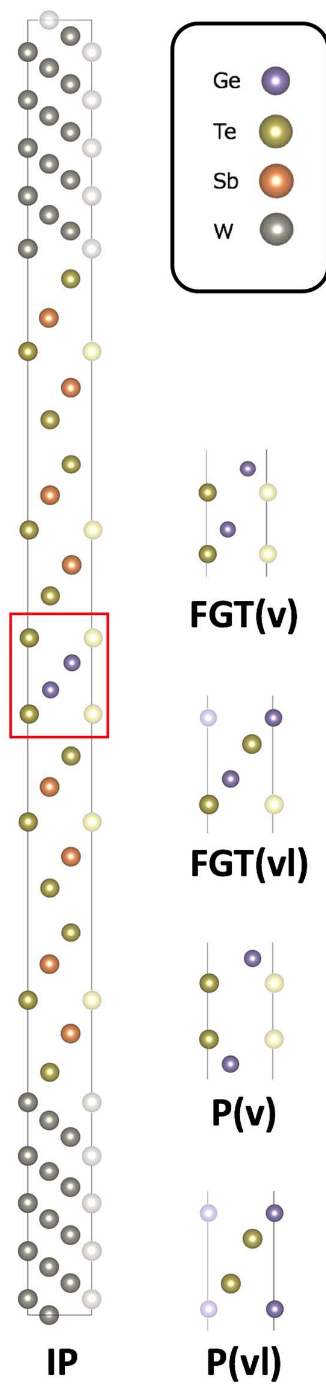

Figure 2

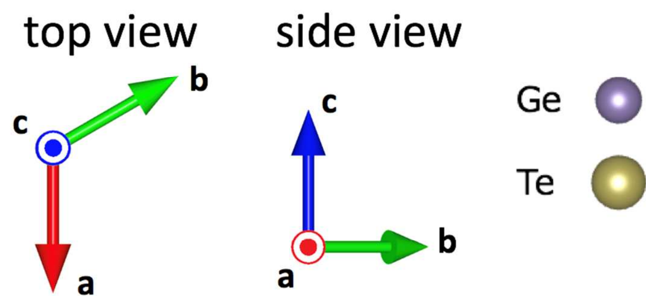

Figure 3 (a)

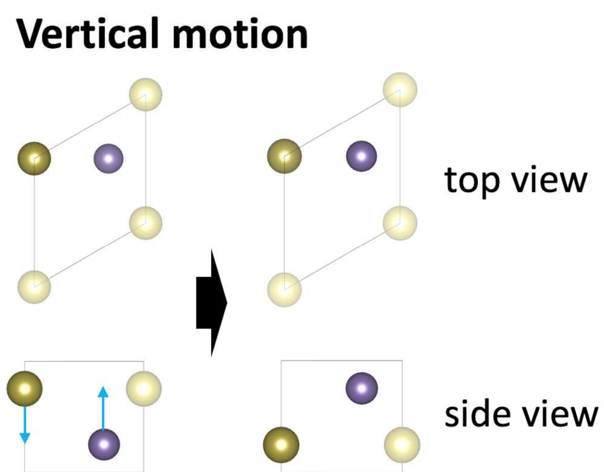

Figure 3 (b)

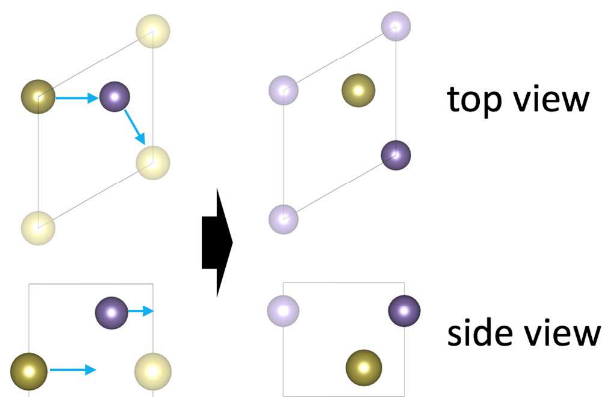

Figure 3 (c)

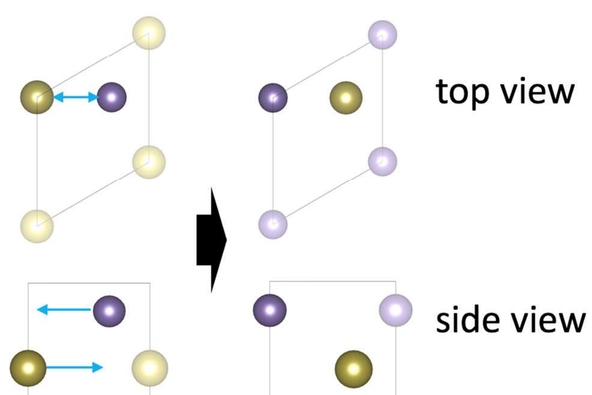

Figure 3 (d)

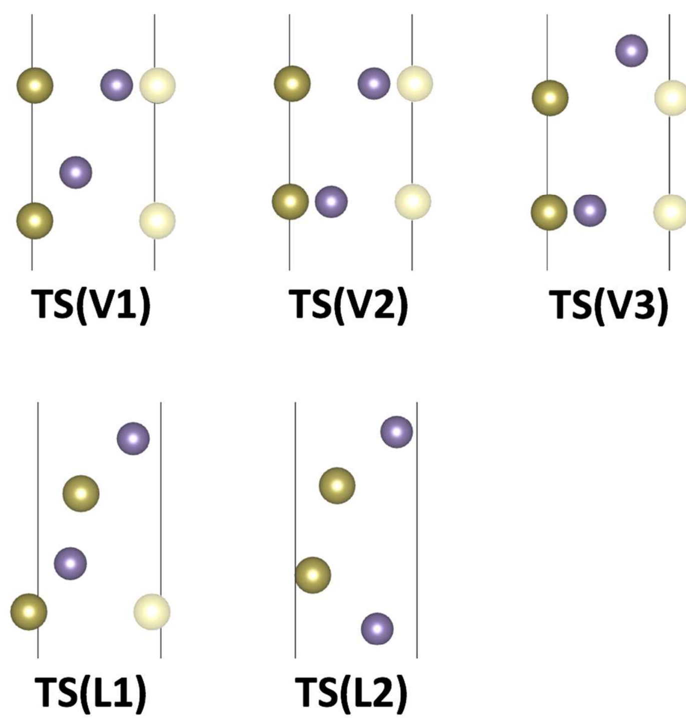

Figure 4

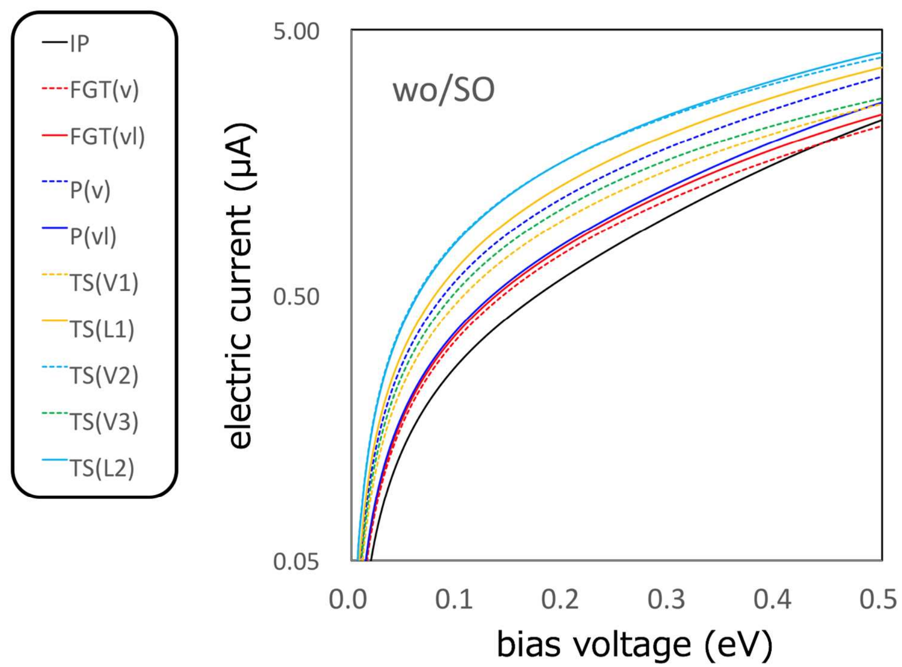

Figure 5 (a)

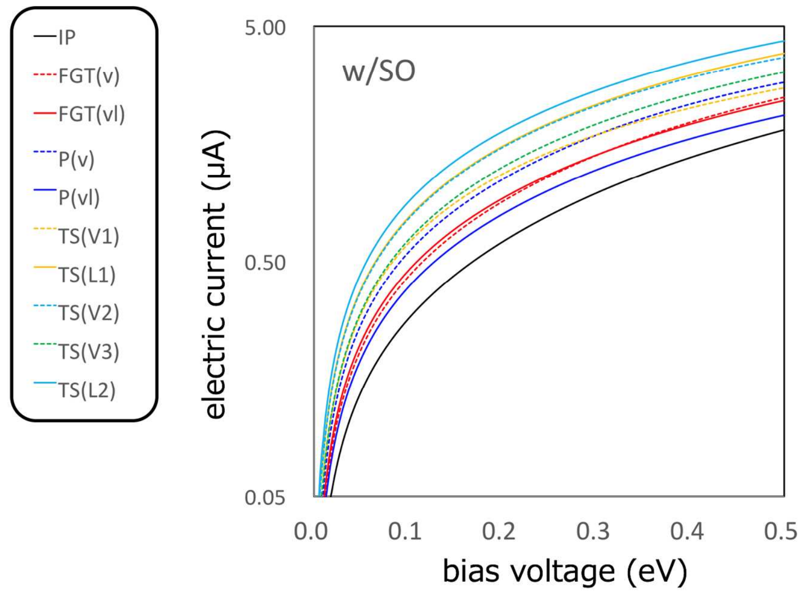

Figure 5 (b)

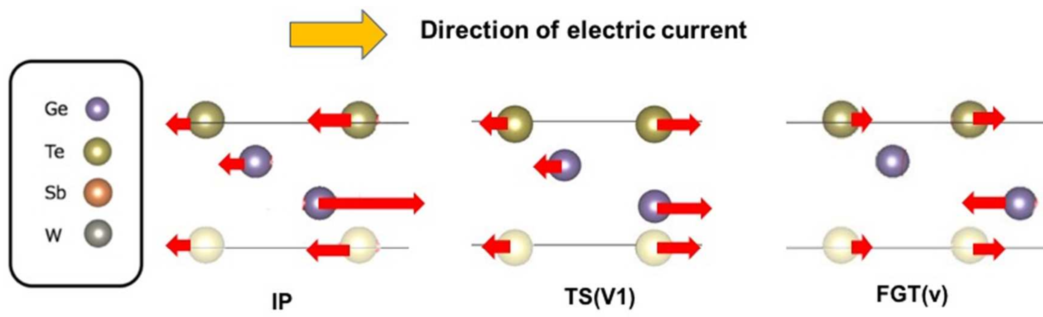

Figure 6